

Impact of hole-doping on the thermoelectric properties of pyrite FeS₂

Anustup Mukherjee* and Alaska Subedi

CPHT, CNRS, École Polytechnique, Institut Polytechnique de Paris, 91128 Palaiseau, France

(Dated: November 8, 2024)

We present a comprehensive first-principles analysis of the thermoelectric transport properties of hole-doped pyrite FeS₂ that includes electron-phonon interactions. This work was motivated by the observed variations in the magnitude of thermopower reported in previous experimental and theoretical studies of hole-doped FeS₂ systems. Our calculations reveal that hole-doped FeS₂ exhibits large positive room-temperature thermopower across all doping levels, with a room-temperature thermopower of 608 $\mu\text{V}/\text{K}$ at a low hole-doping concentration of 10^{19} cm^{-3} . This promising thermopower finding prompted a comprehensive investigation of other key thermoelectric parameters governing the thermoelectric figure of merit ZT . The calculated electrical conductivity is modest and remains below 10^5 S/m at room-temperature for all doping levels, limiting the achievable power factor. Furthermore, the thermal conductivity is found to be phonon driven, with a high room-temperature lattice thermal conductivity of 40.5 W/mK . Consequently, the calculated ZT remains below 0.1, suggesting that hole-doped FeS₂ may not a viable candidate for effective thermoelectric applications despite its promising thermopower.

I. INTRODUCTION

The need of the hour is to use sustainable materials for energy applications, and FeS₂ in its pyrite form is a promising candidate. It has an indirect band gap of 0.95 eV [1, 2], which has motivated different scientific groups to investigate the electronic and transport properties of self- and impurity-doped FeS₂ for photovoltaic [3–5], battery [6], and thermoelectric [7, 8] applications. Various dopants such as 3d transition metals [8–12], halogens [13] and pnictogens [11, 13, 14] have been used to optimize the transport properties of pyrite FeS₂ by controlling the carrier concentration and nature of the charge carrier.

Over the years, the thermoelectric properties of electron-doped FeS₂ have been extensively studied through both experimental and theoretical investigations [8, 10, 12, 15, 16]. However, electron doping has proven to be an ineffective strategy for enhancing thermoelectric performance. Experimental data consistently show relatively low thermopower (S) in electron-doped FeS₂. The majority experimental studies on Co-doped and low-mobility natural n-type samples exhibit room-temperature S below $-100 \mu\text{V}/\text{K}$ [8–10, 15, 17], although two studies on natural n-type samples have reported absolute room-temperature S values in the range of 300–400 $\mu\text{V}/\text{K}$ [7, 18]. The relatively low value of S in electron-doped FeS₂ is primarily attributed to the presence of a highly dispersive band at the bottom of the conduction band manifold in the electronic structure of FeS₂, resulting in low density of states (DOS) and consequently reduced S . In contrast, the electronic structure of FeS₂ reveals multiple flat bands near the valence band edge, contributing to a high DOS in this region [5, 19–22]. These heavy bands and increased DOS may result in larger S and, consequently, a higher thermoelectric figure of merit

because $ZT \propto S^2$. Therefore, it is reasonable to anticipate that hole-doped pyrite FeS₂ could exhibit promising thermoelectric properties. Despite this potential, there is a relative scarcity of experimental and theoretical studies exploring the electronic and thermoelectric properties of hole-doped FeS₂.

A density functional theory (DFT) study by Gudelli *et al.* reported a large thermopower of approximately 750 $\mu\text{V}/\text{K}$ at a hole concentration of 10^{19} cm^{-3} for temperatures up to 800 K, with a reduction to 375 $\mu\text{V}/\text{K}$ at 900 K due to bipolar conduction [16]. Another DFT study by Harran *et al.* predicted a large S of up to 567 $\mu\text{V}/\text{K}$ for hole concentrations of 5×10^{19} to $1 \times 10^{20} \text{ cm}^{-3}$ below 500 K, and a ZT of ~ 0.212 at room-temperature for a doping level of 10^{20} cm^{-3} [20]. Even in undoped samples, experimental studies have observed relatively large positive thermopower, possibly due to defects and impurities present on the surfaces of samples. Karguppikar and Vedeshwar found natural p-type samples exhibiting S between 430–660 $\mu\text{V}/\text{K}$ [18]. Others have reported more modest values of S . Uhlig *et al.* measured S of 128 $\mu\text{V}/\text{K}$ at room temperature in nanoscale pyrite FeS₂ [8], while Rehman *et al.* observed S of 119 $\mu\text{V}/\text{K}$ at 373 K in lab-grown pyrite FeS₂ nanoparticles [23]. Harada *et al.* and Zuñiga-Puelles *et al.* reported positive S below 300 K, followed by a change of sign at higher temperatures, leading to large negative values [24, 25]. These significant variations in measured S underscore the need for a more detailed investigation into the thermoelectric transport properties of hole-doped pyrite FeS₂.

In this paper, we examine the thermoelectric properties of hole-doped pyrite FeS₂ using first-principles calculations that incorporate scattering processes due to electron-phonon interactions. We find positive S below 400 K across all examined hole concentrations, with a maximum room-temperature S of approximately 608 $\mu\text{V}/\text{K}$ at the lowest studied hole doping level (10^{19} cm^{-3}). S changes sign due to bipolar conduction effects in the investigated temperature range, except for the

* Contact: anustup.mukherjee@polytechnique.edu

highest doping level. Electrical conductivity (σ) exhibits a non-monotonic trend, initially decreasing with temperature before increasing at higher temperatures, also influenced by bipolar conduction. The room-temperature σ remains around 10^5 S/m irrespective of the doping level, with a value of ~ 470 S/m at hole doping level of 10^{19} cm $^{-3}$. Our calculations taking account the electron-phonon and three-phonon interactions indicate that the thermal conductivity is predominantly phonon-driven, with the lattice contribution (κ_{ph}) exceeding 40 W/mK at room-temperature, while the electronic thermal conductivity (κ_e) remains below 0.15 W/mK across all doping levels at 300 K. We obtain a reasonably good power factor (PF) at 100 K, but relatively low PF between 300–700 K for low doping levels. The thermoelectric figure of merit remains below 0.1 across all temperatures and doping levels, primarily due to low electrical conductivity and high lattice thermal conductivity, as ZT is proportional to $\sigma/(\kappa_e + \kappa_{ph})$. Despite the promisingly high value of thermopower, the overall low ZT suggests that hole-doped pyrite FeS $_2$ is unlikely to exhibit high thermoelectric efficiency. While our calculations provide valuable insights into the thermoelectric properties of hole-doped pyrite FeS $_2$, experimental investigations are crucial to validate these theoretical predictions and explore potential avenues for improving its thermoelectric performance.

II. COMPUTATIONAL DETAILS

We performed density functional theory calculations using the QUANTUM ESPRESSO (QE) package [26–28]. The exchange-correlation part of the Hamiltonian was approximated by the GGA scheme of Perdew, Burke, and Ernzerhof [29]. We employed the ultrasoft pseudopotentials with core corrections obtained from PSLIBRARY (v.1.0.0) [30]. The valence shell electronic configurations of the pseudopotentials were $3d^64s^2$ (Fe) and $3s^23p^4$ (S). A converged kinetic energy and charge density cut-off of 60 and 600 Ry were taken for the self-consistent cycles, respectively. A Γ -centered k -point mesh of $12 \times 12 \times 12$ was used for the self-consistent calculation. The energy convergence criterion was set to 10^{-14} Ry.

To calculate the phonon dispersion and the second-order interatomic force constants, we employed density functional perturbation theory (DFPT) implemented in the QE code. We used a Γ -centered q -point mesh of $4 \times 4 \times 4$ to obtain the dynamical matrices. This mesh is consistent with the k -point mesh used for non-self-consistent calculation, as required by the PERTURBO code [31] to calculate the transport properties. PERTURBO solves the semiclassical Boltzmann transport equation (BTE) taking electron-phonon (e-ph) interactions into account. Within the Boltzmann transport theory, the

BTE for a periodic system is formulated as:

$$\frac{\partial f_{nk}(r, t)}{\partial t} = -[\nabla_r f_{nk}(r, t) \cdot v_{nk} + \hbar^{-1} \nabla_k f_{nk}(r, t) \cdot F] + I[f_{nk}], \quad (1)$$

where $f_{nk}(r, t)$, t , k , r , n , v_{nk} , \hbar , F and $I[f_{nk}]$ are the electron occupations, time, crystal momentum, spatial coordinate, band index, band velocities, reduced Planck's constant, external fields, and collision integral, respectively. The collision integral is given by:

$$I[f_{nk}] = -\frac{2\pi}{\hbar} \frac{1}{N_q} \sum_{mqv} |g_{mqv}(k, q)|^2 \times [\delta(\epsilon_{nk} - \hbar\omega_{vq} - \epsilon_{mk+q}) \times F_{em}] \times [\delta(\epsilon_{nk} + \hbar\omega_{vq} - \epsilon_{mk+q}) \times F_{abs}], \quad (2)$$

where N_q , q , $|g_{mqv}(k, q)|$, and v represent the number of q -points used for the summation, phonon wavevector, e-ph matrix elements, and mode index, respectively. The electron quasiparticles and phonon energies are given as ϵ_{nk} and $\hbar\omega_{vq}$. F_{em} and F_{abs} represent the phonon emission and absorption terms, respectively.

PERTURBO reads the results of DFT and DFPT calculations performed on coarse k - and q -point grids and then expresses the electron energies, phonon frequencies and e-ph matrix elements in the Wannier basis. Transport properties are calculated by interpolating these quantities on fine k - and q -point grids and using them in the solution of the BTE. We used an interpolation factor of 80 and performed a uniform sampling of the first Brillouin zone using 500,000 random q -points to obtain the relaxation time τ_{nk} . We then applied the relaxation time approximation (RTA) to calculate S , σ and κ_e . The conductivity and Seebeck tensors are given by:

$$\sigma_{\alpha\beta} = e^2 \int dE (-\partial f^0 / \partial E) \sum_{\alpha\beta} (E) \quad (3)$$

$$[\sigma S]_{\alpha\beta} = \frac{e}{T} \int dE (-\partial f^0 / \partial E) (E - \mu) \sum_{\alpha\beta} (E). \quad (4)$$

Here S is the Seebeck coefficient and $\sum_{\alpha\beta} (E)$ is the transport distribution function (TDF), which is defined as:

$$\sum_{\alpha\beta} (E) = \frac{s}{N_k \Omega} \sum_{nk} v_{nk}^\alpha F_{nk}^\beta \delta(E - \epsilon_{nk}), \quad (5)$$

where e is the electronic charge, α and β are the Cartesian directions, f^0 represents the equilibrium Fermi-Dirac distribution, μ is the chemical potential, T is the temperature, s represents the spin degeneracy, Ω is unit cell volume, and $F_{nk} = \tau_{nk} v_{nk}$ in the RTA approach.

The third-order force constants used in the calculation of the lattice contribution to thermal conductivity was obtained using the THIRORDER.PY code [32]. We used a $3 \times 3 \times 3$ supercell to generate an irreducible set of atomic

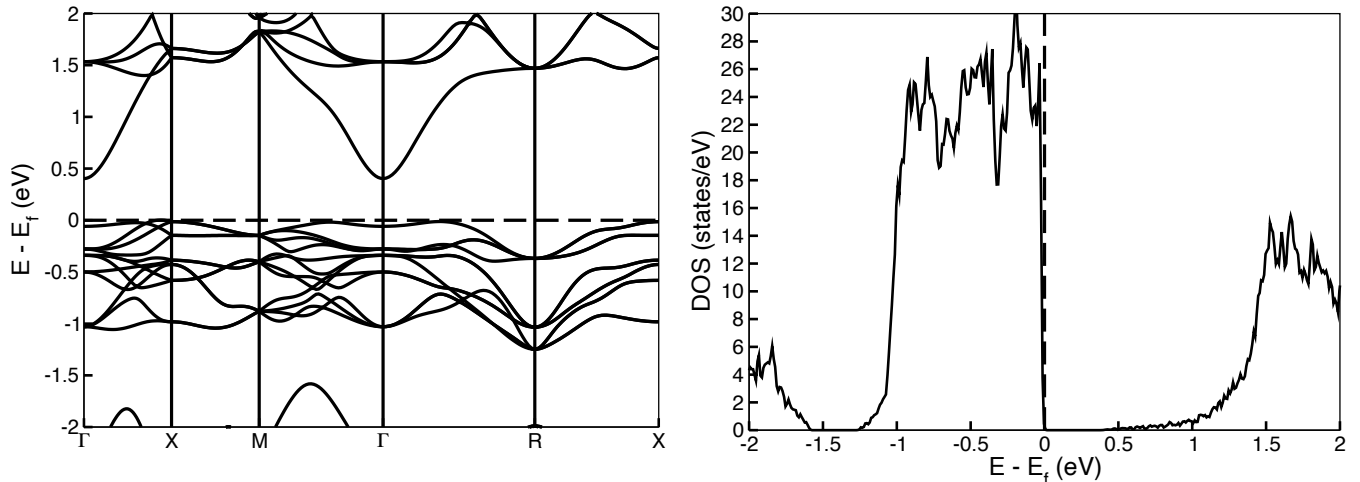


FIG. 1. (Left) Electronic band structure and (right) density of states of stoichiometric FeS₂. The Fermi energy is shifted to the valence band maximum.

displacements up to the third nearest neighbour. Self-consistent DFT runs were performed on the generated set to obtain the atomic forces, which were then used to calculate the third-order force constants. The lattice thermal conductivity was then calculated by solving the Boltzmann transport equation for phonons within RTA using the ShengBTE package [32, 33]. κ_{ph} within BTE is formulated as:

$$\kappa_l^{\alpha\beta} = \frac{1}{k_b T^2 \Omega N} \sum_{\lambda} f_0(f_0 + 1) (\hbar\omega_{\lambda})^2 v_{\lambda}^{\alpha} F_{\lambda}^{\beta}, \quad (6)$$

where k_b , N , f_0 , ω_{λ} , λ , and v_{λ}^{α} are Boltzmann's constant, number of q -points, Bose-Einstein distribution function, angular frequency, phonon mode, and group velocity, respectively. $F_{\lambda}^{\beta} = \tau_{\lambda}^0 v_{\lambda}^{\beta}$ is the linearized BTE within RTA and τ_{λ}^0 is the relaxation time of the phonon mode λ .

III. STRUCTURAL DETAILS

Pyrite FeS₂ adopts a cubic crystal structure, with a space group of $Pa\bar{3}$, with four formula units per unit cell. The Fe and S atoms occupy distinct crystallographic sites and their relative positions are governed by a single structural parameter u . For our calculations, we used an experimentally determined lattice constant of $a = 5.407$ Å, as reported in previous studies [34, 35]. The atomic positions were then obtained by minimizing the atomic forces to less than 10^{-6} Ry/Bohr. The optimized value for u , which governs all the bond distances, was found to be 0.3827.

IV. RESULTS AND DISCUSSIONS

A. Electronic Structure

Numerous density functional theory studies have previously explored the electronic structure of stoichiometric FeS₂ [1, 5, 19, 22, 34, 36]. These calculations consistently reveal multiple heavy bands near the valence band edge that are composed of nominally Fe t_{2g} orbitals, as well as a highly dispersive band at the bottom of the conduction band manifold featuring a mix of Fe e_g and S p character. Consequently, high electronic density of states are observed near the valence band edge, while the conduction band region shows a relatively lower DOS. In Fig. 1, we reproduce the band structure and DOS of FeS₂ in the left and right columns, respectively. Our calculations yield an indirect band gap of 0.40 eV using the PBE functional, which is in reasonable agreement with the 0.52 eV band gap reported by Harran *et al.* using the HSE functional [20]. However, our computed band gap is lower than the 0.95 eV value reported in previous experimental studies [1, 2].

B. Transport Properties

We first look at the temperature-dependent thermopower S of hole-doped FeS₂ across various doping levels, as shown in Fig. 2. Our calculations indicate a consistent behaviour in S for hole doping concentrations (n_h) at and below 1×10^{20} cm⁻³. Initially, S increases with increasing temperature. However, at higher temperatures, it begins to decrease, eventually reaching large negative values due to occupation of dispersive conduction band across the gap. With further increase in temperature, S becomes less negative within this doping range. For n_h of 5×10^{20} cm⁻³, the Fermi level now lies deeper. Conse-

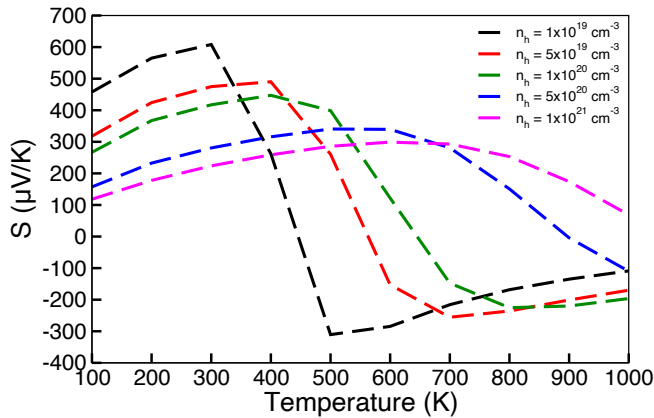


FIG. 2. Seebeck coefficient S of hole-doped FeS_2 in the concentration range 10^{19} – 10^{21} cm^{-3} .

TABLE I. Room temperature thermopower S and electrical conductivity σ of hole-doped FeS_2 at doping concentrations n_h ranging from 10^{19} – 10^{21} cm^{-3} .

n (cm^{-3})	S ($\mu\text{V}/\text{K}$)	$\sigma \times 10^2$ (S/m)
1×10^{19}	608.12	4.72
5×10^{19}	474.72	23.71
1×10^{20}	417.10	46.27
5×10^{20}	280.53	220.88
1×10^{21}	223.70	416.16

quently, S becomes negative above only above 800 K. A similar behaviour in S is also reported in several experiments [24, 25]. In contrast, for the highest n_h considered in this study (1×10^{21} cm^{-3}), S remains positive within the investigated temperature range. However, we predict S to change its sign for this doping level at higher temperatures when bipolar conduction becomes dominant. The room-temperature S values for the studied hole doping levels are reported in Table I. The maximum room-temperature S of 608 $\mu\text{V}/\text{K}$ occurs, as expected, for the lowest doping concentration of 1×10^{19} cm^{-3} . With further increase in hole doping, the room-temperature S decreases gradually but remains positive. This behaviour can be rationalized by observing the electronic structure of FeS_2 . As more holes are introduced in the system, the Fermi energy shifts deeper in the valence band manifold where the bands are more dispersive. This increases particle-hole symmetry, thereby reducing S . Since the calculated values of S are promising, with room-temperature S exceeding 200 $\mu\text{V}/\text{K}$ across all studied n_h values, we extend our analysis to the additional transport parameters that govern ZT .

The calculated room-temperature σ for all doping levels are summarized in Table I, and they show the expected increase in σ as a function of n_h . Fig. 3 shows the temperature dependence of σ for various hole doping levels. We find that σ shows a similar trend as a

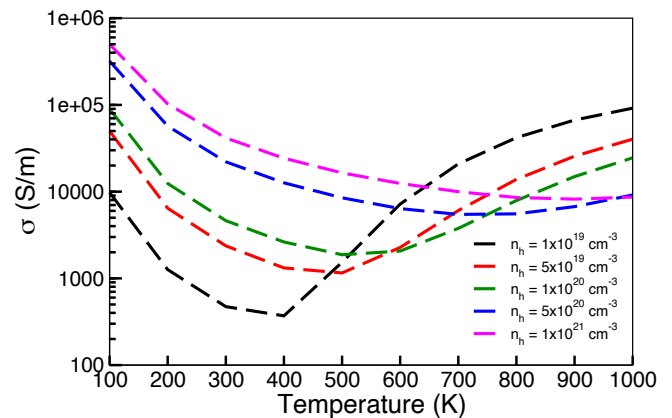


FIG. 3. Electrical conductivity σ of hole-doped FeS_2 in the concentration range 10^{19} – 10^{21} cm^{-3} .

function of n_h at and below 1×10^{20} cm^{-3} . Initially, σ decreases with increasing temperature. However, further increase in temperature leads to upturn in σ due to increased population of the dispersive conduction band. As the doping concentration is increased, the upturn in σ occurs at higher values. For n_h of 1×10^{19} cm^{-3} , the upturn happens at 400 K, where as σ starts increasing only above 800 K for n_h of 5×10^{20} cm^{-3} . The increase in the population of the dispersive conduction band at high temperatures also leads to high-temperature σ being larger for low doping levels that is observed in Fig. 3. Meanwhile, the Fermi level lies deeper for the highest considered n_h of 1×10^{21} cm^{-3} . Consequently, the dispersive conduction band is less occupied for this case, and its σ decreases continuously with temperature, with only a moderate increase observed above 900 K.

We have so far discussed the temperature dependence of S and σ only in terms of the relative difference in the dispersion of the heavy valence and light conduction

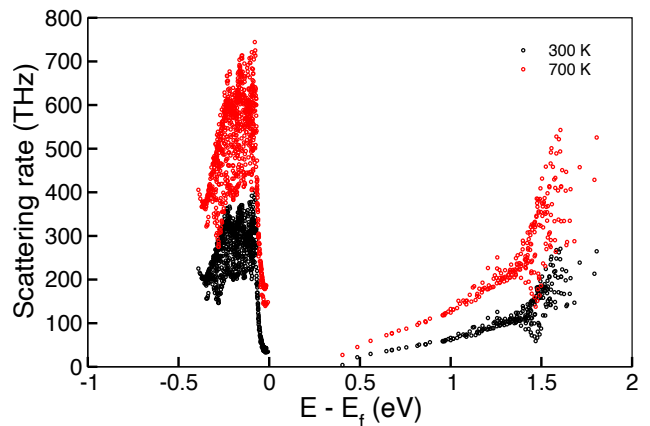


FIG. 4. Electron-phonon scattering rates (the inverse of relaxation time) as a function of energy at 300 and 700 K for carrier concentration $n_h = 1 \times 10^{19}$ cm^{-3} . The Fermi energy is shifted to the valence band maximum.

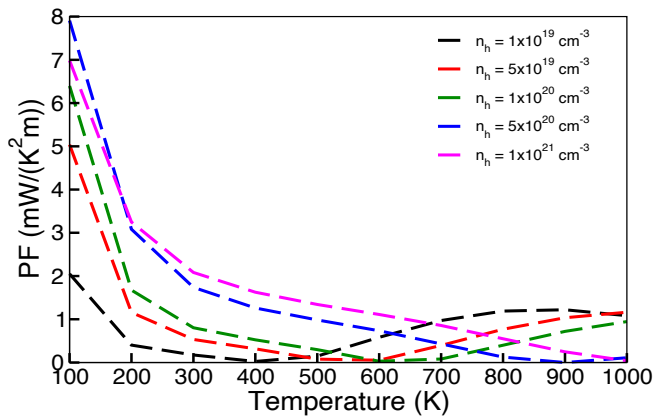


FIG. 5. Power factor of hole-doped FeS₂ in the concentration range 10^{19} – 10^{21} cm⁻³.

bands near Fermi level. The relaxation time τ_{nk} of the carriers in these bands is another microscopic quantity that could play a role in the temperature dependence of these physical quantities. Fig. 4 shows the calculated el-ph scattering rates ($= 1/\tau_{nk}$) at 300 K and 700 K for n_h of 1×10^{19} cm⁻³. At 300 K, the e-ph scattering rates near the valence band edge are higher compared to those at the conduction band minimum. At 700 K, the scattering rates increase for both sets of bands, but the increase is much larger in the valence band manifold. The scattering rates of the states near the valence band edge are now around an order of magnitude larger than those near the conduction band edge. This large asymmetry likely causes the large jump in S to negative values at high temperatures. The relatively low values of scattering rate in the conduction band manifold also contributes to the increase in σ at high temperatures.

Following the observation of high values of calculated S , we investigated the power factor at the corresponding hole concentrations, which is shown in Fig. 5 as a function of temperature. At 100 K, the PF is reasonably high, ex-

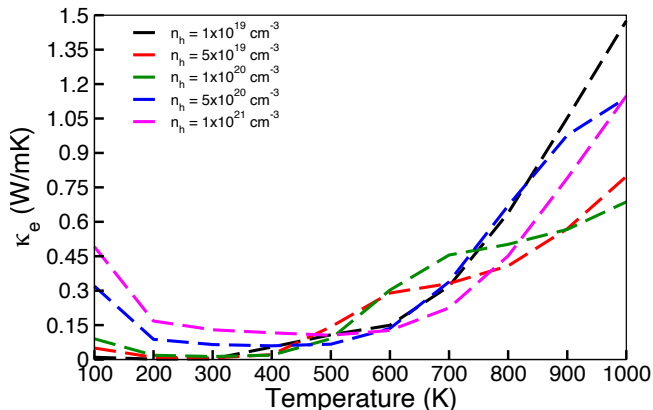


FIG. 6. Electronic thermal conductivity κ_e of hole-doped FeS₂ in the concentration range 10^{19} – 10^{21} cm⁻³.

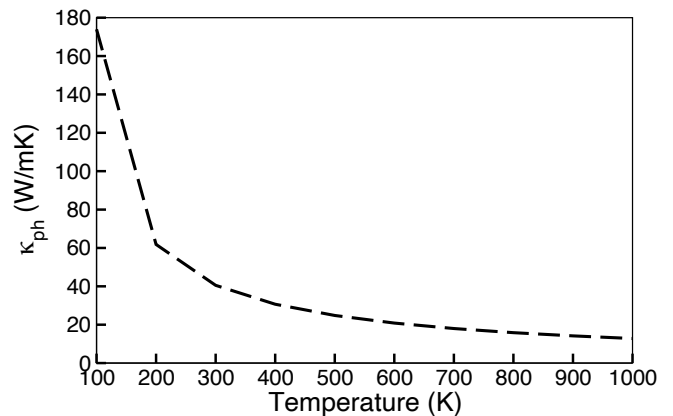


FIG. 7. Lattice thermal conductivity κ_{ph} of stoichiometric FeS₂ taking into account three-phonon scattering interactions.

ceeding 2 mW/K²m across all doping levels. This can be attributed to the moderately high conductivity at 100 K, given that PF is proportional to σ . However, for doping concentrations ranging between 10^{19} and 10^{20} cm⁻³, the PF decreases and remains below 1 mW/K²m within the temperature range of 300 to 600 K. In this temperature range, σ remains below 10^5 S/m, and S undergoes a sign change, leading to low PF values. Only at the highest n_h of 1×10^{21} cm⁻³, the PF exceeds 1 mW/K²m up to 600 K. Additionally, at 1000 K, we observe PF values close to 1 mW/K²m for lower doping concentrations ($\leq 1 \times 10^{20}$ cm⁻³), which can be attributed to the increase in σ and the large negative S observed at this temperature.

Calculation of the thermoelectric figure of merit ZT additionally requires the knowledge of thermal conductivity. The electronic contribution to thermal conductivity κ_e across all doping levels is shown in Fig. 6. Our calculations reveal that κ_e is relatively low, and remains below 1.5 W/mK across the entire temperature range studied. Since the relatively small values of hole doping concentration considered here is should only modestly change the phonon dispersions, we calculated the computationally demanding lattice contribution to thermal conductivity κ_{ph} only for the undoped FeS₂, which is shown in Fig. 7. In contrast to κ_e , κ_{ph} is significantly higher, reaching a maximum of approximately 174 W/mK at 100 K. The room-temperature κ_{ph} is around 40.5 W/mK, whereas κ_e reaches a maximum of 0.13 W/mK at the same temperature for a hole doping concentration of 1×10^{21} cm⁻³. This suggests that the thermal conductivity is predominantly phonon-driven at these temperatures. Our calculated room-temperature κ_{ph} is in close agreement with previous experimental finding of 47.8 ± 2.4 W/mK on single-crystal FeS₂ [37], and is lower than the 65.8 W/mK value reported in a previous theoretical study [38]. However, a recent experimental investigation reported a lattice thermal conductivity of approximately 22–24 W/mK at room-temperature in FeS₂ samples grown via chemical vapor transport (CVT) [39].

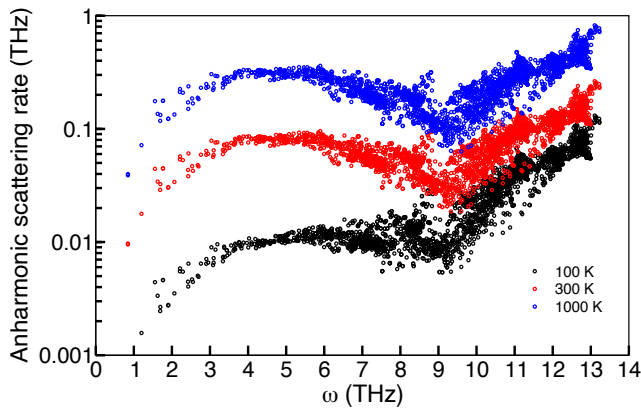


FIG. 8. Anharmonic scattering rates of stoichiometric FeS₂ at temperatures of 100, 300 and 1000 K.

This discrepancy could be attributed to the presence of vacancies and surface impurities in the CVT-grown samples.

The high values of κ_{ph} at low temperatures can be understood through an examination of anharmonic scattering rates. Fig. 8 illustrates the three-phonon contribution to anharmonic scattering rates obtained at 100, 300 and 1000 K. Our calculations show that anharmonic scattering rates increase with temperature across the entire frequency spectrum. However, this increase is particularly pronounced in the low to intermediate frequency region (below 8 THz). Since low frequency phonons are the primary carriers of heat, this substantial temperature-induced increase in scattering rates results in a rapid decrease in κ_{ph} as temperatures is increased. Our calculated room-temperature scattering rates predominantly lie in the range of 0.01–0.1 THz, comparable to those observed in skutterudites like CoSb₃ and IrSb₃ that also exhibit room-temperature κ_{ph} values above 10 W/mK [40]. In contrast, the skutterudite compound FeSb₃ shows significantly higher room-temperature scat-

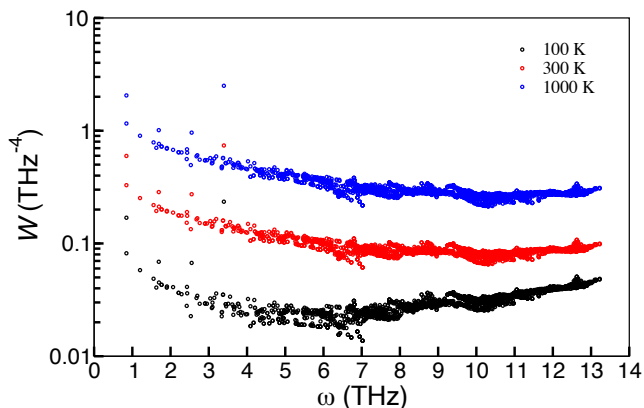


FIG. 9. Weighted phase space W of stoichiometric FeS₂ at 100, 300 and 1000 K.

tering rates (0.1–10 THz), leading to an ultralow room-temperature κ_{ph} of 1.14 W/mK [41]. This comparison underscores the critical role of scattering rates in determining thermal transport properties. Our observation of the increased scattering rates at higher temperatures is further supported by the behaviour of the weighted phase space (W), as shown in Fig. 9. W exhibits a similar temperature-dependent increase across the entire frequency range. This increase in W indicates a greater availability of three-phonon scattering channels at elevated temperatures, which contributes to the observed reduction in κ_{ph} at elevated temperatures.

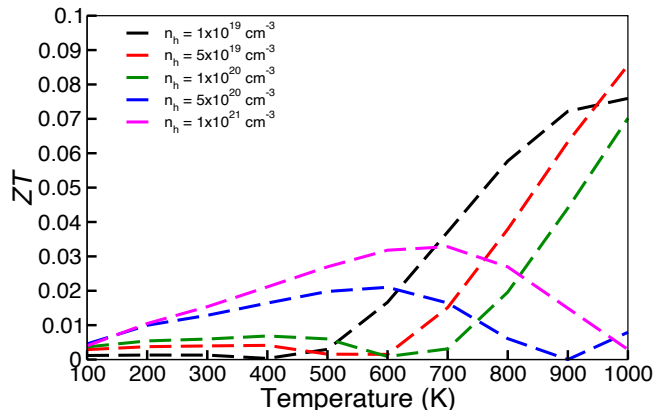


FIG. 10. Thermoelectric figure of merit ZT of hole-doped FeS₂ in the concentration range 10^{19} – 10^{21} cm⁻³.

The thermoelectric figure of merit ZT as a function of temperature obtained using the calculated S , σ , and κ is presented in Fig. 10. ZT is less than 0.01 at low temperatures for all doping concentrations. Such low values can be attributed to the large lattice thermal conductivity obtained at low temperatures. As the temperature increases, ZT shows a moderate increase up to 500 K for doping values between 10^{19} and 10^{20} cm⁻³, consistent with their low PF. At even higher temperatures, their ZT increases due to a combination of increasing PF and decreasing κ_{ph} . For concentrations above 10^{20} cm⁻³, ZT gradually increases with temperature, reaching a maximum between 600–700 K, and subsequently decreases due to the low PF. However, for hole doping at 5×10^{20} cm⁻³, a moderate increase in ZT is observed above 900 K, which follows a similar increase in its PF. The room-temperature ZT is small, with a maximum of 0.015 for the highest doping level of 1×10^{21} cm⁻³. We obtain a highest ZT of approximately 0.086 for hole concentration of 5×10^{19} cm⁻³ at 1000 K. Our maximum calculated ZT is lower than $ZT \sim 0.212$ at room temperature calculated by Harran *et al.* without taking into account electron-phonon scattering [20].

V. CONCLUSIONS

In this study, we investigated the thermoelectric transport properties of hole-doped pyrite FeS₂, incorporating electron-phonon interactions across a wide doping range using first-principles calculations. This research was motivated by previous theoretical findings that revealed multiple heavy bands near the valence band edge in stoichiometric FeS₂, as well as subsequent reports of significant variations in thermopower in hole-doped FeS₂ from both experimental and theoretical perspectives.

Our investigation of hole-doped pyrite FeS₂ revealed complex thermoelectric behavior across various doping levels and temperatures. We observed a maximum positive S of approximately 608 $\mu\text{V}/\text{K}$ at room temperature for the lowest doping level. Notably, bipolar conduction induced a sign change in S at higher temperatures for all but the highest doping level. This bipolar conduction effect was also observed in the electrical conductivity, which, while moderately high at room temperature, remained below 10^5 S/m. The highest observed σ was approximately 5×10^5 S/m for the highest doping level at 100 K. Due to significant variations in S and moderate σ values, the power factor was relatively low above room temperature, exceeding 2 mW/K²m only at the lowest

temperatures across all doping levels. We find that thermal transport in the system is dominated by phonon contributions, with lattice thermal conductivity exhibiting remarkably high values below room temperature, including a room-temperature κ_{ph} of 40.5 W/mK. This results from reduced anharmonic scattering rates and limited phase space availability at low temperatures. In contrast, the electronic contribution to the thermal conductivity remains low across all temperatures, consistently below 1.5 W/mK. The modest values of electrical conductivity and relatively high values of thermal conductivity lead to low ZT of less than 0.1. This suggests that hole-doped pyrite FeS₂ is unlikely to be an effective material for thermoelectric applications even though it exhibits high calculated thermopower. So alternative doping strategies that improve electrical conductivity and degrade thermal conductivity should be explored to make this material viable for thermoelectric application.

ACKNOWLEDGMENTS

We express our gratitude to Sylvie Hébert and David J. Singh for useful discussions. This work was supported by Agence Nationale de la Recherche under grant ANR-21-CE50-0033 and GENCI-TGCC under grant A0170913028.

-
- [1] A. Schlegel and P. Wachter, Optical properties, phonons and electronic structure of iron pyrite FeS₂, *Journal of Physics C: Solid State Physics* **9**, 3363 (1976).
 - [2] A. Ennaoui, S. Fiechter, H. Goslowsky, and H. Tributsch, Photoactive synthetic polycrystalline pyrite FeS₂, *Journal of The Electrochemical Society* **132**, 1579 (1985).
 - [3] A. Ennaoui, S. Fiechter, C. Pettenkofer, N. Alonso-Vante, K. Büker, M. Bronold, C. Höpfner, and H. Tributsch, Iron disulfide for solar energy conversion, *Sol. Energy Mater. Sol. Cells* **29**, 289 (1993).
 - [4] Y. Tomm, R. Schieck, K. Ellmer, and S. Fiechter, Growth mechanism and electronic properties of doped pyrite FeS₂ crystals, *J. Crystal Growth* **146**, 271 (1995), vapour Growth and Epitaxy 1994.
 - [5] V. Eyert, K.-H. Höck, S. Fiechter, and H. Tributsch, Electronic structure of FeS₂: The crucial role of electron-lattice interaction, *Phys. Rev. B* **57**, 6350 (1998).
 - [6] E. Strauss, D. Golodnitsky, and E. Peled, Study of phase changes during 500 full cycles of Li/composite polymer electrolyte/FeS₂ battery, *Electrochim. Acta* **45**, 1519 (2000).
 - [7] K. Kato, Y. Okamoto, J. Morimoto, and T. Miyakawa, The thermoelectric properties of FeS₂, *J. Mater. Sci. Lett.* **16**, 914 (1997).
 - [8] C. Uhlig, E. Guenes, A. S. Schulze, M. T. Elm, P. J. Klar, and S. Schlecht, Nanoscale FeS₂ (pyrite) as a sustainable thermoelectric material, *J. Electron. Mater.* **43**, 2362 (2014).
 - [9] B. Thomas, K. Ellmer, W. Bohne, J. Röhrich, M. Kunst, and H. Tributsch, Photoeffects in cobalt doped pyrite FeS₂ films, *Solid State Commun.* **111**, 235 (1999).
 - [10] P. Díaz-Chao, I. Ferrer, and C. Sánchez, Co distribution through n-type pyrite thin films, *Thin Solid Films* **516**, 7116 (2008).
 - [11] S. Lehner, K. Savage, and J. Ayers, Vapor growth and characterization of pyrite FeS₂ doped with Co, Ni, and As: Variations in semiconducting properties, *J. Cryst. Growth* **286**, 306 (2006).
 - [12] A. Mukherjee and A. Subedi, Thermoelectric transport properties of electron-doped pyrite FeS₂, *J. Phys. Chem. C* **128**, 6573 (2024).
 - [13] J. Hu, Y. Zhang, M. Law, and R. Wu, First-principles studies of the electronic properties of native and substitutional anionic defects in bulk iron pyrite, *Phys. Rev. B* **85**, 085203 (2012).
 - [14] B.-H. Lei and D. J. Singh, Ferromagnetism in a semiconductor with mobile carriers via low-level nonmagnetic doping, *Phys. Rev. Appl.* **15**, 044036 (2021).
 - [15] J. Clamagirand, J. Ares, E. Flores, P. Diaz-Chao, F. Leardini, I. Ferrer, and C. Sánchez, Influence of temperature on thermoelectric properties of Fe_xCo_{1-x}S₂ thin films: A semiconductor to semimetal conversion, *Thin Solid Films* **600**, 19 (2016).
 - [16] V. K. Gudelli, V. Kanchana, S. Appalakondaiah, G. Vaitheeswaran, and M. C. Valsakumar, Phase stability and thermoelectric properties of the mineral FeS₂: An ab initio study, *J. Phys. Chem. C* **117**, 21120 (2013).
 - [17] G. Willeke, O. Blenk, C. Kloc, and E. Bucher, Preparation and electrical transport properties of pyrite FeS₂ single crystals, *J. Alloys Compd.* **178**, 181 (1992).

- [18] A. M. Karguppikar and A. G. Vedeshwar, Electrical and optical properties of natural iron pyrite FeS_2 , *Phys. Stat. Sol. (a)* **109**, 549 (1988).
- [19] G. L. Zhao, J. Callaway, and M. Hayashibara, Electronic structures of iron and cobalt pyrites, *Phys. Rev. B* **48**, 15781 (1993).
- [20] I. Harran, Y. Li, H. Wang, Y. Chen, and Y. Ni, Iron disulfide compound: a promising thermoelectric material, *Materials Research Express* **4**, 105907 (2017).
- [21] W. Folkerts, G. A. Sawatzky, C. Haas, R. A. de Groot, and F. U. Hillebrecht, Electronic structure of some 3d transition-metal pyrites, *Journal of Physics C: Solid State Physics* **20**, 4135 (1987).
- [22] A. Mukherjee and A. Subedi, Minority-spin conducting states in Fe substituted pyrite CoS_2 , *J. Phys.: Condens. Matter* **36**, 025501 (2023).
- [23] U. Rehman, J. Jacob, K. Mahmood, A. Ali, A. Ashfaq, M. Basit, N. Amin, S. Ikram, S. Hussain, H. Noor, A. ul Ahmad, and N. ur Rehman, Improving the thermoelectric performance of hydrothermally synthesized FeS_2 nanoparticles by post sulfurization, *Ceramics International* **46**, 20496 (2020).
- [24] T. Harada, Transport properties of iron dichalcogenides FeX_2 ($X = \text{S}, \text{Se}$ and Te), *J. Phys. Soc. Japan* **67**, 1352 (1998).
- [25] E. Zuñiga-Puelles, R. Cardoso-Gil, M. Bobnar, I. Veremchuk, C. Himcinschi, C. Hennig, J. Kortus, G. Heide, and R. Gumeniuk, Structural stability and thermoelectric performance of high quality synthetic and natural pyrites (FeS_2), *Dalton Trans.* **48**, 10703 (2019).
- [26] P. Giannozzi, S. Baroni, N. Bonini, M. Calandra, R. Car, C. Cavazzoni, D. Ceresoli, G. L. Chiarotti, M. Cococcioni, I. Dabo, A. D. Corso, S. de Gironcoli, S. Fabris, G. Fratesi, R. Gebauer, U. Gerstmann, C. Gougoussis, A. Kokalj, M. Lazzeri, L. Martin-Samos, N. Marzari, F. Mauri, R. Mazzarello, S. Paolini, A. Pasquarello, L. Paulatto, C. Sbraccia, S. Scandolo, G. Sclauzero, A. P. Seitsonen, A. Smogunov, P. Umari, and R. M. Wentzcovitch, Quantum espresso: a modular and open-source software project for quantum simulations of materials, *Journal of Physics: Condensed Matter* **21**, 395502 (2009).
- [27] P. Giannozzi, O. Andreussi, T. Brumme, O. Bunau, M. B. Nardelli, M. Calandra, R. Car, C. Cavazzoni, D. Ceresoli, M. Cococcioni, N. Colonna, I. Carnimeo, A. D. Corso, S. de Gironcoli, P. Delugas, R. A. DiStasio, A. Ferretti, A. Floris, G. Fratesi, G. Fugallo, R. Gebauer, U. Gerstmann, F. Giustino, T. Gorni, J. Jia, M. Kawamura, H.-Y. Ko, A. Kokalj, E. Küçükbenli, M. Lazzeri, M. Marsili, N. Marzari, F. Mauri, N. L. Nguyen, H.-V. Nguyen, A. O. de-la Roza, L. Paulatto, S. Poncé, D. Rocca, R. Sabatini, B. Santra, M. Schlipf, A. P. Seitsonen, A. Smogunov, I. Timrov, T. Thonhauser, P. Umari, N. Vast, X. Wu, and S. Baroni, Advanced capabilities for materials modelling with quantum espresso, *Journal of Physics: Condensed Matter* **29**, 465901 (2017).
- [28] P. Giannozzi, O. Baseggio, P. Bonfà, D. Brunato, R. Car, I. Carnimeo, C. Cavazzoni, S. de Gironcoli, P. Delugas, F. Ferrari Ruffino, A. Ferretti, N. Marzari, I. Timrov, A. Urru, and S. Baroni, Quantum ESPRESSO toward the exascale, *The Journal of Chemical Physics* **152**, 154105 (2020).
- [29] J. P. Perdew, K. Burke, and M. Ernzerhof, Generalized gradient approximation made simple, *Phys. Rev. Lett.* **77**, 3865 (1996).
- [30] A. Dal Corso, Pseudopotentials periodic table: From H to Pu, *Comput. Mater. Sci* **95**, 337 (2014).
- [31] J.-J. Zhou, J. Park, I.-T. Lu, I. Maliyov, X. Tong, and M. Bernardi, Perturbo: A software package for ab initio electron-phonon interactions, charge transport and ultrafast dynamics, *Comput. Phys. Commun* **264**, 107970 (2021).
- [32] W. Li, L. Lindsay, D. A. Broido, D. A. Stewart, and N. Mingo, Thermal conductivity of bulk and nanowire $\text{Mg}_2\text{Si}_x\text{Sn}_{1-x}$ alloys from first principles, *Phys. Rev. B* **86**, 174307 (2012).
- [33] W. Li, J. Carrete, N. A. Katcho, and N. Mingo, Shengbte: A solver of the boltzmann transport equation for phonons, *Comput. Phys. Commun* **185**, 1747 (2014).
- [34] K. Umemoto, R. M. Wentzcovitch, L. Wang, and C. Leighton, Electronic structure of $\text{Co}_{1-x}\text{Fe}_x\text{S}_2$, *Phys. Status Solidi b* **243**, 2117 (2006).
- [35] R. W. G. Wyckoff, *Crystal Structures - Volume 1*. (New York: Interscience., 1963).
- [36] Z.-Y. Feng, Y. Yang, and J.-M. Zhang, The structural, electronic and magnetic properties of $\text{Co}_{1-x}\text{Fe}_x\text{S}_2$, *Mater. Res. Express* **5**, 016507 (2018).
- [37] P. A. Popov, P. P. Fedorov, and S. V. Kuznetsov, Thermal conductivity of FeS_2 pyrite crystals in the temperature range 50-300 K, *Crystallogr. Rep.* **58**, 319 (2013).
- [38] T. Jia, X. Liu, Y. Zhang, and S.-H. Wei, Origin of the variation in lattice thermal conductivities in pyrite-type dichalcogenides, *Phys. Rev. B* **107**, 115204 (2023).
- [39] A. Özden, E. Zuñiga-Puelles, J. Kortus, R. Gumeniuk, and C. Himcinschi, Thermal conductivity and phonon anharmonicity of chemical vapor transport grown and mineral- FeS_2 single crystals: An optothermal raman study, *J Raman Spectrosc* **54**, 84 (2023).
- [40] W. Li and N. Mingo, Lattice dynamics and thermal conductivity of skutterudites CoSb_3 and IrSb_3 from first principles: Why IrSb_3 is a better thermal conductor than CoSb_3 , *Phys. Rev. B* **90**, 094302 (2014).
- [41] Y. Fu, D. J. Singh, W. Li, and L. Zhang, Intrinsic ultralow lattice thermal conductivity of the unfilled skutterudite FeSb_3 , *Phys. Rev. B* **94**, 075122 (2016).